PAPER • OPEN ACCESS

Quantum state transfer via acoustic edge states in a 2D optomechanical array

New Journal of Physics
The open access journal at the forefront of physics

Deutsche Physikalische Gesellschaft DPG
IOP Institute of Physics

Published in partnership with: Deutsche Physikalische Gesellschaft and the Institute of Physics

OPEN ACCESS

RECEIVED
19 July 2019

REVISED
15 October 2019

ACCEPTED FOR PUBLICATION
28 October 2019

PUBLISHED
14 November 2019

PAPER

Quantum state transfer via acoustic edge states in a 2D optomechanical array

Marc-Antoine Lemonde[1], **Vittorio Peano**[2], **Peter Rabl**[3] **and Dimitris G Angelakis**[1,4]

[1] Centre for Quantum Technologies, National University of Singapore, 3 Science Drive 2, Singapore 117543, Singapore
[2] Max Planck Institute for the Science of Light, Staudtstrasse 2, D-91058 Erlangen, Germany
[3] Vienna Center for Quantum Science and Technology, Atominstitut, TU Wien, A-1040 Vienna, Austria
[4] School of Electrical and Computer Engineering, Technical University of Crete, Chania, Crete, 73100, Greece

E-mail: cqtml@nus.edu.sg

Keywords: topology, silicon-vacancy, optomechanics, phononic network, quantum state transfer, solid-state physics

Supplementary material for this article is available online

Abstract

We propose a novel hybrid platform where solid-state spin qubits are coupled to the acoustic modes of a two-dimensional array of optomechanical (OM) nano cavities. Previous studies of coupled OM cavities have shown that in the presence of strong optical driving fields, the interplay between the photon-phonon interaction and their respective inter-cavity hopping allows the generation of topological phases of sound and light. In particular, the mechanical modes can enter a Chern insulator phase where the time-reversal symmetry is broken. In this context, we exploit the robust acoustic edge states as a chiral phononic waveguide and describe a state transfer protocol between spin qubits located in distant cavities. We analyze the performance of this protocol as a function of the relevant system parameters and show that a high-fidelity and purely unidirectional quantum state transfer can be implemented under experimentally realistic conditions. As a specific example, we discuss the implementation of such topological quantum networks in diamond based OM crystals where point defects such as silicon-vacancy centers couple to the chiral acoustic channel via strain.

1. Introduction

In recent years the efforts towards building scalable quantum information processing devices have reached unprecedented intensities. For this purpose, a number of physical platforms, such as superconducting circuits [1], cold atoms in optical lattices [2, 3], trapped ions [4], Rydberg atoms [5] and defect centers in solids [6–10], are actively investigated. In parallel, various strategies for implementing hybrid quantum systems are currently explored [11–13], with the long-term goal to combine the strengths of the different architectures and to mitigate system-specific weaknesses. In this context, high-Q mechanical elements play a particularly important role for realizing coherent quantum interfaces [14–21] as they can be coupled efficiently to a large variety of other quantum systems [22] while being themselves only weakly affected by decoherence. Similar to optical fields, acoustic waves can be guided along coupled resonator arrays or continuous phononic waveguides [23–25], which can be used to implement chip-scale quantum networks where quantum information is distributed via individual propagating phonons [23, 26–29]. In particular, such phononic quantum channels have been proposed to overcome the problem of coherently integrating a large number of electronic spin qubits associated with defect centers in diamond [14, 28, 30–34]. However, being in its infancy, the control of acoustic waves on the quantum level still faces many challenges, which must be met both on an experimental and on a conceptual level. This includes, for example, the scattering of phonons along the channel by fabrication imperfections, but even more fundamentally, the ability to emit phonon wavepackets with a specified shape and direction, as a prerequisite for many quantum state transfer protocols [35].

In this work we propose and analyze an hybrid phononic quantum network, where spin qubits or other two-level systems (TLS) are coherently coupled to the chiral acoustic edge channels of a two dimensional (2D)

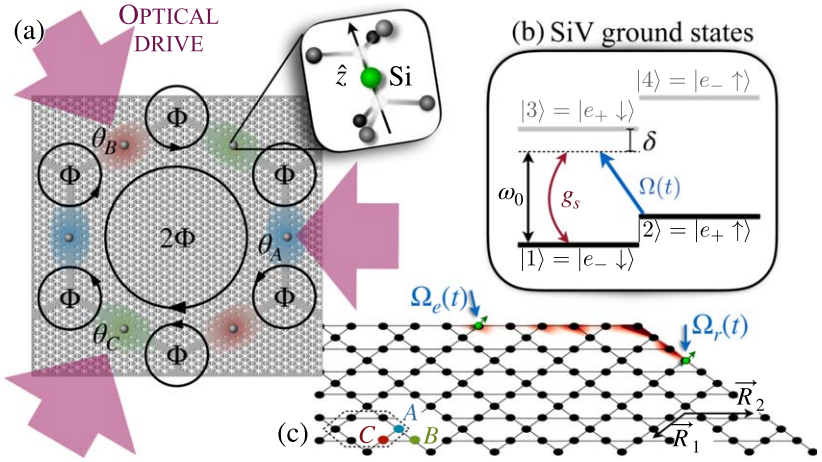

Figure 1. Schematics of the 2D hybrid system and the state transfer protocol. (a) OM cavities engineered from smooth alterations of a snowflake-hole patterning in diamond. The cavities are arranged in a Kagome structure where the unit cells include a basis of three sites $s = \{A, B, C\}$. A TLS is embedded in every site. The phase pattern $\{\theta_s\}$ induced by the optical driving generates a flux Φ upon hopping anti-clockwise through a unit cell. (b) Energy structure of the SiV ground-state subspace where the two lowest-energy states $|1\rangle$ and $|2\rangle$ form a long-lived spin qubit. A microwave drive $\Omega(t)$ couples opposite spin states while the strain associated with a single phonon couples the orbital degrees of freedom $|e_\pm\rangle$ with strength g_s. The combination of the two processes leads to a tunable interaction between the spin states and phonons of frequency $\sim\omega_0$. (c) State transfer between distant TLS via topologically protected chiral acoustic waves propagating along the boundaries of the structure.

optomechanical (OM) array [36–41]. This architecture is motivated by the progress in engineering spin-phonon interactions in solid-state systems [42–49], as well as in fabricating 2D OM crystals [50–53] with different geometries and band structures. In a previous work [54] it has been shown that 2D OM arrays can exhibit a rich set of topological phases of sound and light that can be fully explored by tuning *in situ* the optical driving of the cavities. In particular, for weak OM interactions, the acoustic excitations are expected to enter a Chern insulator phase where chiral edge states propagate along the array boundaries. Thus this hybrid quantum system offers a platform to study rich physics emerging from the interplay between spins, mechanical and optical degrees of freedom in phases where time-reversal symmetry is broken.

As a first application for this setup we focus on the quantum-state transfer between TLS located in distant cavities via chiral acoustic edge channels. Compared to state transfer protocols in regular 1D phononic waveguides [23, 26, 28, 29], this platform offers the advantages of a unidirectional propagation [35, 55–57], which is robust against local perturbations and where the direction can be controlled by external optical driving fields. While the basic protocol discussed in this work is very general, a naturally-suited system where these ideas can be implemented is an array of separated silicon vacancy (SiV) centers in a diamond OM crystal. In this case, quantum information can be stored in the long-lived spin degrees of freedom of the SiV ground state [58–62], where at low temperatures of $T \lesssim 1$ K coherence times exceeding $T_2 \sim 10$ ms have been demonstrated [61, 62]. At the same time the orbital degrees of freedom of the defect allow strong and tunable coupling to vibrational modes, as recently discussed in [28]. Combined with the ability to design chiral acoustic channels via OM interactions this coherent spin-phonon interface offers many new tools to overcome fundamental challenges in phononic quantum network applications.

2. Model

We consider a 2D array of OM cavities as depicted in figure 1, where each lattice site contains a single TLS. The OM array can be realized, for example, in so-called 'snowflake' structures [63], where high-Q vibrational and optical modes are co-localized in regions of engineered defects created by smoothly varying the size of the patterned periodic snowflake holes (see figure 1(a)).

At each lattice site j, the variation in the index of refraction due to mechanical vibrations leads to a strong OM coupling that can be described by the standard OM Hamiltonian $\hat{H}_{\rm OM}/\hbar = \omega_M \hat{b}_j^\dagger \hat{b}_j + \omega_c \hat{a}_j^\dagger \hat{a}_j + g_0 \hat{a}_j^\dagger \hat{a}_j (\hat{b}_j + \hat{b}_j^\dagger)$ [64]. Here $\hat{a}_j$ ($\hat{b}_j$) represents the annihilation operator of the photonic (phononic) mode of frequency ω_c (ω_M) and g_0 is the OM coupling per photon. Due to the strong localization of both photons and phonons, this coupling can reach values of about $g_0 \sim 250$ kHz [52], which we will assume for all the following estimates. The optical cavities are driven by a strong external laser field of frequency ω_L, which drives each optical mode into a coherent state with amplitude $\alpha_j(t) = \sqrt{n_c} e^{i\theta_j} e^{-i\omega_L t}$, where $n_c \gg 1$ is the mean intracavity photon

number. By redefining $a_j \rightarrow a_j + \alpha_j(t)$, the OM interactions can be linearized and in a frame rotating with ω_L, the resulting Hamiltonian for the whole 2D OM array is given by ($\hbar = 1$)

$$\hat{H}_{\mathrm{OMC}} = \sum_j (\omega_M \hat{b}_j^\dagger \hat{b}_j - \Delta \hat{a}_j^\dagger \hat{a}_j + G e^{i\theta_j} \hat{a}_j^\dagger \hat{b}_j + G e^{-i\theta_j} \hat{b}_j^\dagger \hat{a}_j) + \sum_{\langle i,j \rangle} (K \hat{b}_i^\dagger \hat{b}_j + J \hat{a}_i^\dagger \hat{a}_j + \mathrm{h.c.}). \quad (1)$$

Here $J > 0$ ($K > 0$) denotes the nearest-neighbor photon (phonon) hopping rate and $\Delta = \omega_L - \omega_C < 0$ is the detuning between the cavities and the drive. In equation (1), $G = g_0 \sqrt{n_c}$ is the linear OM coupling, which is enhanced by the number of photons in a cavity. The sign of J and K depend on the details of the design of the OM defect cavities. The case $J, K < 0$ (without TLS) is discussed in [54]. Here, we explore the different scenario where $J, K > 0$. Below we show that this choice leads to a more favorable scaling of the topological band gaps and the required input power. At this stage, we consider all parameters identical throughout the lattice except for the driving phases θ_j. Note that in equation (1), we made an additional rotating-wave approximation by neglecting processes that do not conserve the number of excitations ($\sim G e^{-i\theta_j} a_j b_j + \mathrm{h.c.}$). The validity of this approximation is discussed in appendix A.

In addition to the localized optical and mechanical modes, we consider a TLS embedded in each sites of the array, which is coupled to the acoustic vibrations via strain. We model the interaction by a Jaynes–Cumming coupling with time-dependent strength $g_{\mathrm{sp}}(t)$, such that the effective Hamiltonian describing the full hybrid 2D array reads

$$\hat{H} = \hat{H}_{\mathrm{OMC}} + \sum_j \frac{\omega_0}{2} \hat{\sigma}_z^{(j)} + \sum_j [g_{\mathrm{sp}}^{(j)}(t) \hat{\sigma}_+^{(j)} \hat{b}_j + \mathrm{h.c.}]. \quad (2)$$

Here ω_0 is the transition frequency of the TLS, $\hat{\sigma}_z$ is the usual Pauli-Z operator and $\hat{\sigma}_-^{(j)} = \hat{\sigma}_+^{(j)\dagger}$ destroys a spin excitation in site j.

While the spin-phonon coupling assumed in Hamiltonian (2) is very generic and could be realized with various types of TLS [16, 22, 26], we explicitly consider the example of SiV centers in diamond in our following analysis. As depicted in figure 1, the electronic ground-state manifold of this center consists of two long-lived spin states denoted by $|1\rangle$ and $|2\rangle$, which can be coupled to a mechanical vibrational mode via a microwave assisted Raman process involving the excited state $|3\rangle$. More precisely, the strength of the time-dependent spin-phonon coupling $g_{\mathrm{sp}}(t) = \Omega(t) g_s / \delta$ and the qubit frequency ω_0 can be externally tuned via the microwave drive amplitude $\Omega(t)$ and detuning δ compared to the state $|3\rangle$, respectively. Here g_s is the intrinsic strain coupling between the state $|1\rangle$ and $|3\rangle$. See appendix B, for more details about SiV defects and their strain coupling.

3. Acoustic edge channels

The main purpose of considering a 2D OM array instead of a simple 1D phononic waveguide is to use the OM interaction for engineering topologically protected acoustic edge channels, along which phonon propagation becomes unidirectional and immune against local disorder. As first proposed in [54], such a scenario can be achieved by imposing a non-trivial pattern of the driving phases θ_j, which mimics the presence of a strong effective magnetic field. Similar to electronic systems in real magnetic fields, the resulting bandstructure of the OM crystal may then exhibit topologically protected bands with a non-trivial Chern number, which for a finite system are associated with left- or right-propagating edge modes. In contrast to [54], we here consider a different band structure which leads to much larger topological gaps in presence of weaker optical driving power.

3.1. Topological phases of sound in an OM Kagome lattice

While chiral acoustic edge channels can be implemented with various different OM lattice geometries, we here exclusively focus on the Kagome lattice for which topological phases of sound and light have already been described in [54]. The Kagome crystal structure (see figure 1) is defined by a triangular Bravais lattice spawned by the unit vectors $\{\vec{R}_1 = -(1, \sqrt{3})a, \vec{R}_2 = (2, 0)a\}$ and a three-cavity basis given by $\{\vec{r}_A = (0, \sqrt{3}/2)a$, $\vec{r}_B = -(1/2, \sqrt{3}/2)a, \vec{r}_C = (1/2, -\sqrt{3}/2)a\}$. Here a is the distance between two adjacent cavities and $\{A, B, C\}$ refer to the different cavities within a unit cell. This structure possesses the full $\mathcal{C}_{6v}$ symmetry of the corresponding Bravais lattice.

In absence of the external driving fields, i.e. $G = 0$, the OM crystal system is time-reversal symmetric and contains six energy bands. The three acoustic (optical) bands are centered around ω_M ($-\Delta$) and have a total width of $6K$ ($-6J$). A zoom in of the non-interacting band structure in a spectral range that includes all acoustic bands but exclude far detuned optical modes is shown in figure 2 (a). We see that the $\mathcal{C}_6$ and time-reversal symmetries impose essential degeneracy at the high-symmetry points of the Brillouin zone, i.e. $\mathbf{K} = (2\pi/3a, 0)$ and $\mathbf{K}' = (\pi/3a, \pi/\sqrt{3}a)$, where Dirac cones are formed, and at $\mathbf{\Gamma} = (0, 0)$, where a quadratic band-crossing point appears. Importantly, one of the optical (mechanical) bands is flat. This feature reflects the existence of localized normal modes describing a standing wave where the six cavities along the edges of the same Wigner–

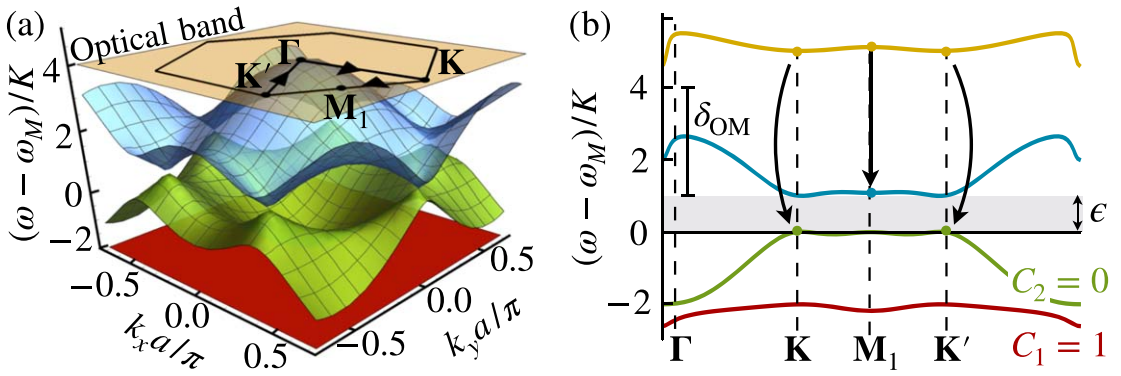

Figure 2. OM band structures. (a) Dispersion relation of the non-interacting OM system ($G = 0$), where the three lowest-energy bands represent mechanical modes while the highest-energy band is optical in nature. The drive detuning here is $\Delta = -\omega_M - 2J - 4K$, which leads to $\delta_{\rm OM} = 3K$, and $J/K = 200$. (b) Dispersion relation along the path $\mathbf{\Gamma} \rightarrow \mathbf{K} \rightarrow \mathbf{M}_1 \rightarrow \mathbf{K}' \rightarrow \mathbf{\Gamma}$ in the Brillouin zone [depicted in (a)] for $G = 2K$, $\delta_{\rm OM} = 3K$ and $J/K = 200$. The black arrows indicate the dominant angular-momentum conserving OM interactions responsible for the gap. The Chern numbers C_l associated with the two lowest-energy mechanical bands are shown.

Seitz cell are excited with equal amplitude but alternating sign. More details about the diagonalization of the OM Hamiltonian in the quasi momentum space are given in appendix C.

For finite driving of the OM cavities ($G \neq 0$) the acoustic and photonic bands hybridize. Following [54], we choose the pattern of phases $\Delta\theta = \theta_B - \theta_A = \theta_C - \theta_B = \theta_A - \theta_C = \pm 2\pi/3$ for every unit cells. In other words, we consider a driving of one of the optical modes at the $\mathbf{\Gamma}$ point. Such phase pattern can be generated by simply using three optical drives pointing at 120° angle from each others [54] (see figure 1(a)). Most importantly, it breaks the time-reversal symmetry without breaking the spatial symmetries of the Kagome lattice and, thus, lifts the essential degeneracies giving rise to topological band gaps [65].

Here, we focus on the weak OM coupling limit where the detuning of all optical modes is larger than the OM coupling, i.e. $G \ll |\omega_M + \Delta + 2J|$, such that all the excitations are still almost phononic or optical in nature. In this regime, the existence of topologically non-trivial phases for sound can be understood from the fact that phonons can also hop to neighboring lattice sites through virtual optical excitations. In the conceptually simplest setting where the optical bandwidth is small compared to the detuning, $J \ll |\omega_M + \Delta|$, this hopping is restricted to nearest neighbors and has an amplitude

$$K_{ij}^{\rm opt} \simeq \frac{G^2 J}{(\omega_M + \Delta)^2} e^{\pm i\Delta\theta_{ij}}. \tag{3}$$

Since the resulting overall phonon hopping amplitude, $K_{ij}^{\rm eff} = K + K_{ij}^{\rm opt}$, then becomes a complex quantity, a phonon moving anti-clockwise around a crystal unit cell basis (i.e. $A \rightarrow B \rightarrow C \rightarrow A$) acquires a phase $\Phi = \pm 3 \arctan \frac{\sqrt{3}JG^2}{JG^2 - 2K(\Delta + \omega_M)^2}$. This is reminiscent of a charged particle moving in a magnetic field where Φ represents the normalized magnetic flux encircled by the three cavities of the basis [66]. Note that the total flux within a Bravais unit cell is zero as moving anti-clockwise over an hexagonal path leads to a phase shift of -2Φ (see figure 1(a)), simulating what is known as the anomalous quantum Hall effect [65]. In a more realistic situation, as considered in this work, the optical hopping rate is larger than the detuning, i.e. $J \gtrsim |\omega_M + \Delta|$. In this case, the same intuition holds but the optically-induced phonon hopping becomes longer-ranged and one must resort to a full numerical evaluation of the band structure, as exemplified in figure 2(b). Finally, in this same limit with $K \ll J$, the corresponding flux $\Phi_{\rm opt}$ experienced by the light field remains negligible, thus suppressing any non-trivial topology of the optical field.

We note in passing that synthetic magnetic fields for vibrations in a phononic crystal can also be generated by purely geometrical means as described in [67]. This scenario is, however, fundamentally different as no breaking of the time-reversal symmetry takes place. This underlying symmetry is imprinted in the magnetic field that has opposite signs in the $\mathbf{K}$ and $\mathbf{K}'$ valleys. This type of time-reversal preserving synthetic magnetic field is usually referred to as a pseudomagnetic field. We emphasize that pseudomagnetic field induced edge states have a time-reversed counter-propagating partner. Therefore, there is no protection against back scattering by lattice scale disorder and a two-level defect will couple to both channels with approximately equal strength.

3.2. Topological gaps

The breaking of time-reversal symmetry opens gaps between the acoustic bands, bringing the vibrational excitations into a Chern insulator phase. This is confirmed by computing the topological invariant, known as the Chern number [66], $C_n = \frac{i}{2\pi}\int_{\rm BZ} d^2\vec{k}\,[\langle\partial_{k_x} m_{\vec{k},n}|\partial_{k_y} m_{\vec{k},n}\rangle - \langle\partial_{k_y} m_{\vec{k},n}|\partial_{k_x} m_{\vec{k},n}\rangle]$ for each acoustic band n with

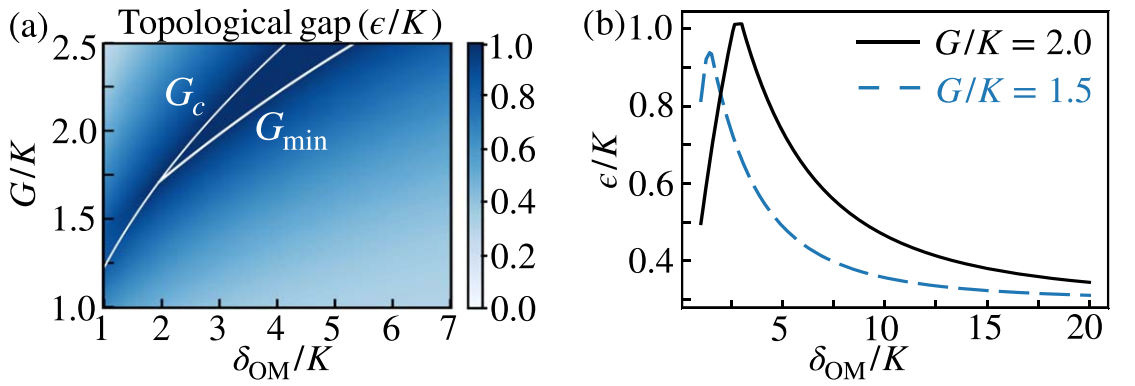

Figure 3. Topological gap. (a) Topological gap size ϵ as a function of G and the detuning $\delta_{\rm OM}$ for $J/K = 200$. The upper white line represents G_c (see equation (5)) and the bottom one shows the minimal OM coupling $G_{\rm min}$ for which ϵ reaches K. (b) Gap size as a function of $\delta_{\rm OM}$ for $G/K = 1.5$ and $G/K = 2.0$ with $J/K = 200$.

energy eigenstates $|m_{\vec{k},n}\rangle$. Here the integral is performed over the first Brillouin zone. For the two lowest-energy mechanical bands, one finds $C_1 = 1$ and $C_2 = 0$ (see figure 2(b)).

As shown in figure 2(b), for weak OM interactions the gaps open at the symmetry points **K** and **K′**, while for larger couplings, competing processes taking place with quasi momentum near the high-symmetry points $\mathbf{M}_1 = \frac{\pi}{2a}\left(1, -\frac{1}{\sqrt{3}}\right)$, $\mathbf{M}_2 = -\frac{\pi}{2a}\left(1, \frac{1}{\sqrt{3}}\right)$ and $\mathbf{M}_3 = \frac{\pi}{a}\left(0, -\frac{1}{\sqrt{3}}\right)$ close the gap again. The dominant OM processes allowed by the conservation of angular momentum can be captured using a simple analytic model from which one accurately predicts the band gap

$$\epsilon = \mathrm{Min}\left[\frac{\delta_{\rm OM}}{2}\left(\sqrt{1 + \frac{4G^2}{\delta_{\rm OM}^2}} - 1\right), K\right], \tag{4}$$

for $G < G_c$, where

$$G_c/K = \sqrt{3\delta_{\rm OM}/2K}, \tag{5}$$

is the critical coupling above which the gap decreases (see appendix D). Here $\delta_{\rm OM} = -\Delta - 2J - \omega_M - K$ is the detuning between the lowest optical band and the mechanical Dirac points in the noninteracting limit (see figure 2(b)).

From the above expressions it follows that the band gap ϵ reaches the maximum value $\epsilon = K$ for a detuning $\delta_{\rm OM}$ above the threshold $\delta_{\rm OM}^{\rm th} = 2K$ and driving strengths in a finite range $G_{\rm min} \leqslant G \leqslant G_c$ where $G_{\rm min} = \sqrt{K^2 + \delta_{\rm OM} K}$. In figure 3(a), we show ϵ as a function of $\delta_{\rm OM}$ and G while explicitly indicating G_c and $G_{\rm min}$. In panel (b), we show ϵ as a function of G for $\delta_{\rm OM}/K = 1.5,\ 2.0$. For experimentally relevant phonon hopping rates $K/2\pi \sim 100$ MHz, the minimal coupling $G_{\rm min} \approx \sqrt{3}K$ at threshold $\delta_{\rm OM}^{\rm th}$ is reached with a number of intra-cavity photons $n_c \sim 0.75 \times 10^6$. While generally challenging, we note that recent experiments suggest that diamond structures [68] are more compliant to stronger drives compared to silicon-based systems [50–53].

3.3. Edge channels

For a finite size system, the existence of separated energy bands with non-trivial Chern number is associated with a set of topologically protected chiral edge states, which propagate along the boundaries of the OM array. Specifically, the difference between the number of such edge states propagating clockwise and anti-clockwise is given by the sum over the topological invariant C_n associated with all lower-energy bands.

To study in more detail the properties of these edge channels in the present setup, we consider in figure 4(a) a stripe of infinite length along x with straight edges at $y = 0$ and $y = -(N_y - 1)\sqrt{3}\,a$. Here N_y is the number of unit cells along $\vec{R}_1$ and the upper straight boundary is obtained by excluding the cavities A of all cells at $y = 0$. For this geometry, the full OM crystal Hamiltonian $\hat{H}_{\rm OMC}$ in equation (1) can be diagonalized within each quasi-momentum k_x subspace, allowing us to capture the dispersion relation and the structure of the edge states localized at the boundaries. Details of the diagonalization are presented in appendix C. In figure 4(b), we show an example of the mechanical band structure as a function of k_x for $G = 2K$, $\delta_{\rm OM} = 3K$ and $\Delta\theta = 3\pi/2$. On the upper boundary, a single edge state is present and its dispersion relation $\omega_E(k_x)$ is shown by the black curve crossing the gap for $\pi/2 < k_x a \leqslant \pi$. The group velocity of phonons propagating along this channel is given by

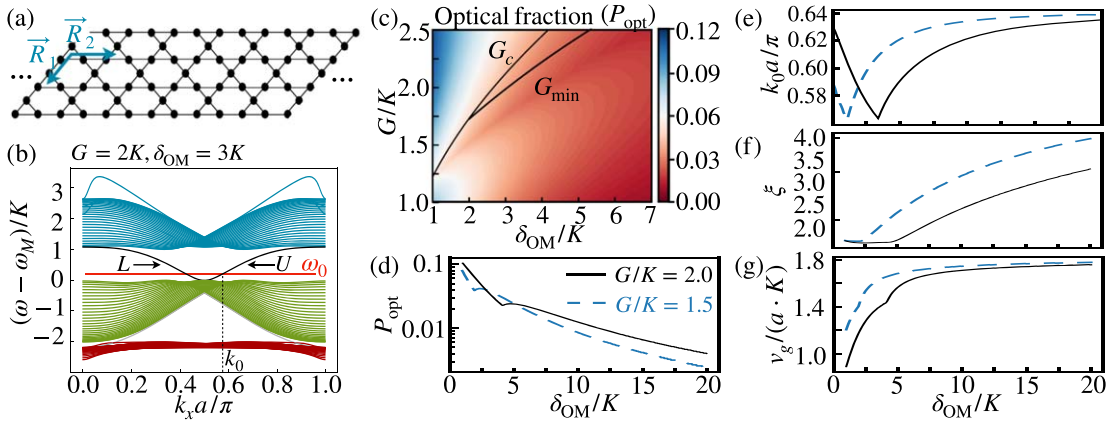

Figure 4. Topologically protected edge states. (a) Schematic of an infinite 1D stripe along x with straight boundaries. (b) An example of the dispersion relation of the OM modes of the infinite stripe with $N_y = 21$ unit cells along $\vec{R}_1$, $G = 2K$ and $\delta_{OM} = 3K$. The edge-state frequencies $\omega_E(k_x)$ are highlighted in black and the resonance frequency of the TLS, ω_0, is shown in red. The edge mode propagating on the upper (lower) edge is labeled U (L). (c) and (d) Optical fraction of the edge state evaluated at k_0 [shown in panel (e)] as a function of G and δ_{OM}. The black lines in (c) indicate the value of G_c and the value of G_{min}. (f) Penetration depth $\xi(k_0)$ of the edge states as a function of δ_{OM} for $G/K = 1.5$ and $G/K = 2.0$. (g) Group velocity v_g of the edge state propagating along the upper boundary ($\pi/2 < k_x a \leqslant \pi$) evaluated at k_0 as a function of δ_{OM} for $G/K = 1.5$ and $G/K = 2.0$. In all figures, the photon hoping is $J/K = 200$.

$$v_g(k_x) = \frac{\partial \omega_E(k_x)}{\partial k_x}, \tag{6}$$

and is positive for the phase pattern $\Delta\theta = 3\pi/2$. The situation is completely symmetric for the edge state at the lower boundary: its energy crosses the gap for $0 < k_x a \leqslant \pi/2$ and it has a negative group velocity.

For the purpose of using such edge modes as phononic quantum channels, two other key properties must be taken into account: their penetration depth into the bulk and how strongly they are hybridized with the optical bands. The latter plays an important role for dissipation and the former characterizes how strongly the edge modes couple to the TLSs. In general, we can write the annihilation operator for an edge-state excitation with quasi-momentum k_x as

$$\hat{b}_E(k_x) = \sum_{s,m} \mathrm{e}^{-\frac{ma}{\xi(k_x)} - \mathrm{i}\phi_m(k_x)} [u_s(k_x)\hat{b}_{s,m}(k_x) + v_s(k_x)\hat{a}_{s,m}(k_x)], \tag{7}$$

where $\hat{b}_{s,m}(k_x)$ [$\hat{a}_{s,m}(k_x)$] is the phononic (photonic) annihilation operator acting on the basis $s = \{A, B, C\}$ of the mth unit cell along $\vec{R}_1$ with quasi-momentum k_x. The upper boundary corresponds to $m = 0$. The coefficients $u_s(k_x)$ and $v_s(k_x)$ are the respective mechanical and optical probability amplitudes, $\xi(k_x)$ is the penetration depth and $\phi_m(k_x)$ is a generic phase. We define the optical fraction of the edge state as

$$P_{opt}(k_x) = \sum_s \frac{|v_s(k_x)|^2}{1 - \mathrm{e}^{-\frac{2a}{\xi(k_x)}}} \leqslant 1, \tag{8}$$

where the upper bound is set by the normalization condition.

In the view of a state transfer between TLS embedded in the outermost cavities along the boundaries of the array, we are mostly interested in the edge-state excitation that lies within the gap and has the smallest penetration depth and photonic amplitude. This condition motivates us to define k_0 such that $u_{s_0}(k_0)$ is maximal (see figure 4(e)), where s_0 represents the outermost cavities along the boundary. In figure 4, we show the optical fraction, the penetration depth $\xi(k_x)$ and the group velocity, all evaluated for $k_x = k_0$. We finally note that for the straight edges considered, i.e. where only the cavities B and C form the outermost layer of the boundaries, no A cavities throughout the crystal supports an edge mode (i.e. $u_A = 0$).

We conclude this section by noting several important differences between the results presented here and those in [54]. In this work, we consider positive hopping amplitudes $K > 0$ and $J > 0$ which results in inverted dispersion relations compared to [54]. As a consequence, the lowest-energy optical band is flat (for $G = 0$). This feature changes qualitatively the OM interaction. In particular, the band gap ϵ and the optical fraction P_{opt} become independent of J for large J/δ_{OM}. In contrast, these quantities are suppressed as $\sqrt{K/J}$ and K/J, respectively, for negative hopping amplitudes [54]. Since $J/K \sim 10^4$ is of the order of the ratio between the speed of light and sound in the material, this allows us to reach much larger band gaps at the expense of larger optical fraction. Finally, for positive hopping amplitudes, the driven optical mode coincides with the lowest-energy band, such that the detuning from the drive frequency is considerably smaller than for the case of the highest-energy band considered in [54]. Due to this reduction of the detuning by about $6J \sim 100$ GHz, the necessary power of the external drive to reach $n_c \sim 10^6$ is strongly reduced.

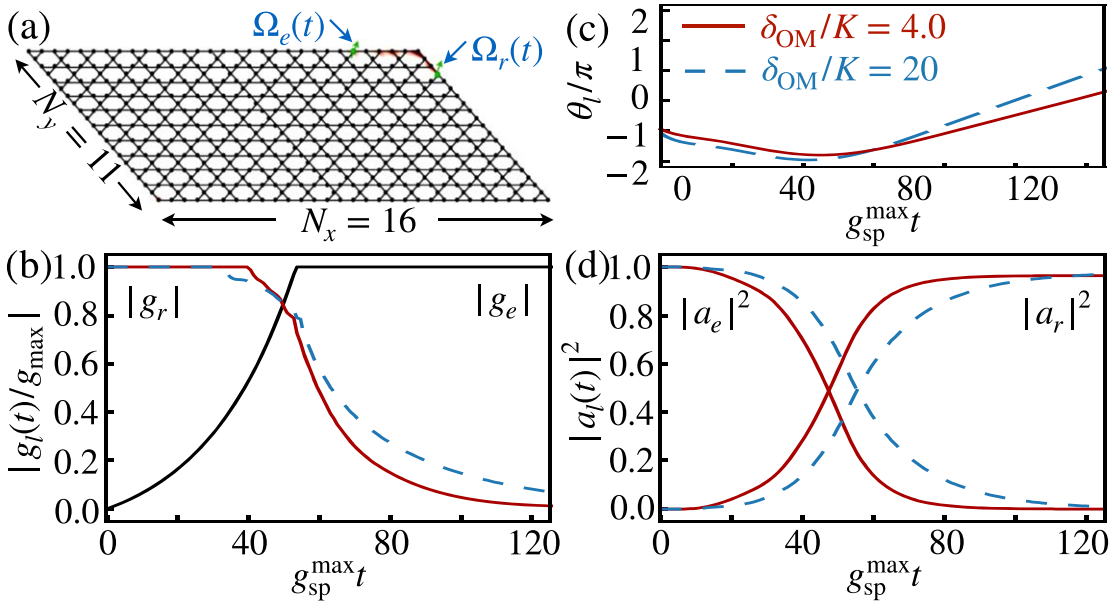

Figure 5. State transfer protocol. (a) Schematic of the state transfer over eight cavities around a corner for two scenarios: (1) $G = 2K$, $\delta_{OM} = 4K$ and $Q_C = 5 \times 10^7$ (solid lines) and (2) $G = 2K$, $\delta_{OM} = 20K$ and $Q_C = 10^7$ (dashed lines). (b) Time dependent coupling rates for the emitting and receiving defects. The emitting pulse is identical in both scenarios (black solid line). (c) The phase of the receiving pulses. (d) Amplitudes of the TLS as a function of time. In all figures, we have considered $\omega_M/K = 460$, $\omega_C/K = 2 \times 10^6$, $J/K = 200$ and $g_{sp}^{max}/K = 0.06$.

4. Quantum state transfer

So far, we have focused solely on the OM cavities without considering finite couplings to the TLS. In this section, we exploit the time-dependent spin-phonon coupling $g_{sp}(t)$ and the acoustic chiral edge states to transfer an arbitrary quantum state between any pairs of TLS embedded in distant cavities along the boundaries of the structure.

In this protocol, only the emitting (e) and receiving (r) defects are driven, i.e. only $g_{sp}^{(l)}(t) \neq 0$ with $l = \{e, r\}$, while all the other undriven centers are far off-resonance with any mechanical excitations. We also consider a low-temperatures environment $T \leqslant \hbar\omega_M/k_B$ (corresponding to $T \lesssim 1$ K for SiV centers) in which case the system remains in the single excitation subspace. Finally, we account for dissipative processes by including photon and phonon loss in every cavities of the crystal. We denote by $\kappa_C = \omega_C/Q_C$ ($\kappa_M = \omega_M/Q_M$) the photon (phonon) decay rate where Q_C (Q_M) is the optical (mechanical) quality factor. By restricting the dynamics to the single-excitation subspace, we can account for losses by simply considering a non-unitary time evolution by substituting $-\Delta \to -\Delta - i\kappa_C/2$ ($\omega_M \to \omega_M - i\kappa_M/2$) in equation (2).

4.1. Markovian channel

In the limit of weak spin-phonon couplings [$g_{sp}^{(l)}(t) \ll K$], the topological phase of sound described in the previous section is approximately unperturbed by the TLS. Moreover, for resonance frequencies ω_0 of both TLS deep within the topological band gap, the defects only couple efficiently to the acoustic edge modes. In this limit, the coherent dynamics of the state transfer protocol can be described by the effective Hamiltonian

$$\hat{H}_{st}(t) = \sum_k \omega_E(k)\hat{b}_E^\dagger(k)\hat{b}_E(k) + \sum_{l=e,r} \frac{\omega_0}{2}\hat{\sigma}_z^{(l)} + \frac{1}{\sqrt{N}}\sum_k \sum_{l=e,r} [g_{eff}^{(l)}(t)\hat{\sigma}_+^{(l)}b_E(k)e^{2ikn_la} + \text{h.c.}], \quad (9)$$

where k and n_l represent the quasi-momentum of the edge state and the position of the TLS l along the edge of N cavities, respectively. The effective spin-phonon coupling $g_{eff}^{(l)}(t) = u_{s_l}(k)e^{-m_la/\xi(k)-i\phi_{m_l}(k)}g_{sp}^{(l)}(t)$ depends on the distance of the defect from the boundary (m_l) and captures the properties of the edge modes previously derived in the context of the semi-infinite stripe. Although the structure supporting the state transfer is a finite 2D crystal (see figure 5(a)), equation (9) is valid for defects positioned far from any dislocations, e.g. a corner. Similarly, one can estimate the decay rate of the chiral channel as $\kappa_E(k) = |u_s|^2\kappa_M/[1 - e^{-2a/\xi(k)}] + P_{opt}(k)\kappa_C$. For the scenarios considered in this work, where the mechanical frequencies are in the GHz regime while the optical modes are in the hundreds of THz, $\kappa_C/\kappa_M \sim \omega_C/\omega_M \sim 10^4$ in cases of similar quality factors. As a consequence, the optically induced decay rate is expected to exceed by far the intrinsic mechanical loss.

Considering the single-excitation ansatz

$$|\psi(t)\rangle = \alpha|0\rangle + \beta e^{-i\omega_0 t}[a_e(t)\hat{\sigma}_+^{(e)} + a_r(t)\hat{\sigma}_+^{(r)} + \sum_k a_k(t)\hat{b}_E^\dagger(k)]|0\rangle, \tag{10}$$

where $|0\rangle$ represents the vacuum state with both centers being in their lowest-energy state and no acoustic excitations in the waveguide, a perfect transfer of an arbitrary state corresponds to $a_e(t_0) = a_r(t_f) = 1$ and $a_e(t_f) = a_r(t_0) = 0$. Here t_0 and t_f are the initial and final times of the protocol, respectively. In the case where the TLS see a constant density of states of the acoustic modes, it is possible the apply the standard Born–Markov approximation to the Schrödinger equation $i\hbar\partial_t|\psi(t)\rangle = \hat{H}_{ss}(t)|\psi(t)\rangle$ (see appendix E), leading to the following local equations of motion

$$\partial_t a_l(t) = -\frac{\gamma_l(t)}{2}a_l(t) - \sqrt{\gamma_l(t)}\,e^{i\theta_l(t)}f_{in,l}(t). \tag{11}$$

Here, the transfer rate between the chiral waveguide and the defects is

$$\gamma_l(t) = 2\frac{|g_{eff}^{(l)}(t)|^2}{v_g/a}, \tag{12}$$

with $v_g \equiv v_g(k_0)$ and $\theta_l(t) = \arg[g_{eff}^{(l)}(t)]$. The input field of the receiving node is $f_{in,r}(t) = f_{out,e}(t-\tau_p)e^{i\phi_p}$ with τ_p and ϕ_p the time and phase acquired during the propagation from the emitter to the receiver. In the case of a perfectly straight edge, $\tau_p = 2(n_r - n_e)a/v_g$ and $\phi_p = k_0 2(n_r - n_e)a$. The strategy to achieve a high-fidelity state transfer is to control in time $g_{eff}^{(r)}(t)$ in order to suppress the output field $f_{out,r}(t) = f_{in,r}(t) + \sqrt{\gamma_r(t)}\,e^{-i\theta_r(t)}a_r(t)$ of the receiver. Thus in this idealized limit, the state transfer-problem becomes equivalent to the scenario discussed in the original work by Cirac *et al* [35] and similar optimized pulse shapes can be used to achieve close-to-unity state transfer fidelities. The main limitation then arises from propagation losses and the ratio between the TLS decoherence rate and the maximal transfer rate γ_{max} that one can reach in a specific implementation.

4.2. Exact evolution

While the above description properly highlights the physics underlying the state-transfer protocol, it becomes exact only for extremely weak couplings to perfect Markovian 1D channels. In contrast, we here perform no approximations and numerically simulate the full dynamics of the time evolution as governed by equation (2). We use a slowly varying pulse for the emitter $g_{sp}^{(e)}(t)/g_{sp}^{max} = \min[1, e^{(t-4)/2}]$ with a weak maximal coupling $g_{sp}^{max}/K = 0.06$. The optimal pulse for the receiver $g_{sp}^{(r)}(t)$ is then determined by maximizing at every time step the amplitude of the receiver $|a_r(t)|$. In figures 5(b)–(d), we show two examples of state transfers over a distance of eight cavities along the edge of a crystal with $N_x = 16$ ($N_y = 11$) unit cells along x (y). Specifically, in both examples the emitter and the receiver are located on different edges of the crystal (see figure 5(a)), such that the non-trivial transfer of excitations around a corner is included in the simulations. We compare two scenarios: the first one with higher cavity quality factor $Q_C = 5.0 \times 10^7$ and strong OM coupling $G = 2K$ with $\delta_{OM} = 4K$; and the second with lower $Q_C = 10^7$ and more detuned OM coupling $G = 2K$ and $\delta_{OM} = 20K$. In the first scenario, the edge state is more localized and has a slower group velocity (see figure 4), leading to a faster state-transfer via a stronger $\gamma_{max}/g_{sp}^{max} \sim 0.03$ (see equation (12)). However, the larger optical hybridization and longer time spent in the waveguide make the optically-induced decay rate more detrimental, hence the need of higher Q_C. In the second scenario, the transfer is slower with $\gamma_{max}/g_{sp}^{max} \sim 0.006$, but more resilient to dissipation.

In figure 6(a), we analyze the maximal fidelity $F = |a_r(t_f)|^2$ as a function of the detuning δ_{OM} for $G = 2K$ for $Q_C = \{0.5, 1.0, 5.0\} \times 10^7$. It highlights the larger optically-induced decay rate for smaller detunings. In the short-time limit, one can approximate the optical loss as $1 - F \sim N_s P_{opt}\kappa_C a/v_g$ with N_s the number of traveled cavities. For larger detunings, the optical loss is reduced, but the smaller decay rates require longer time t_f to transfer the state, which can become an issue compared to the coherence time of the TLS. As an example, for $K/2\pi = 100$ MHz and $g_{sp}^{max}/K = 0.06$, $t_f \sim 2\mu$s for $G = 2K$ and $\delta_{OM} = 4K$. This is still fast compared to the expected inhomogeneous dephasing times $T_2^* \sim$ 10–100 μs and much shorter than the intrinsic coherence time of $T_2 \sim 10$ ms demonstrated for SiV centers at low temperatures.

4.3. Disorder

So far, we have consider identical parameters over the entire system, i.e. perfectly matched mechanical frequencies, detunings and OM couplings. In experiments, reaching a high level of homogeneity is challenging and any realizations is expected to have a certain level of disorder. We here analyze the robustness of the state transfer in presence of such imperfections within the system. To do so, we consider all parameters to be slightly different for every cavities. For example, we consider local disorder such that $\omega_M^{(j)} = (1 + p_j)\omega$ where p_j is

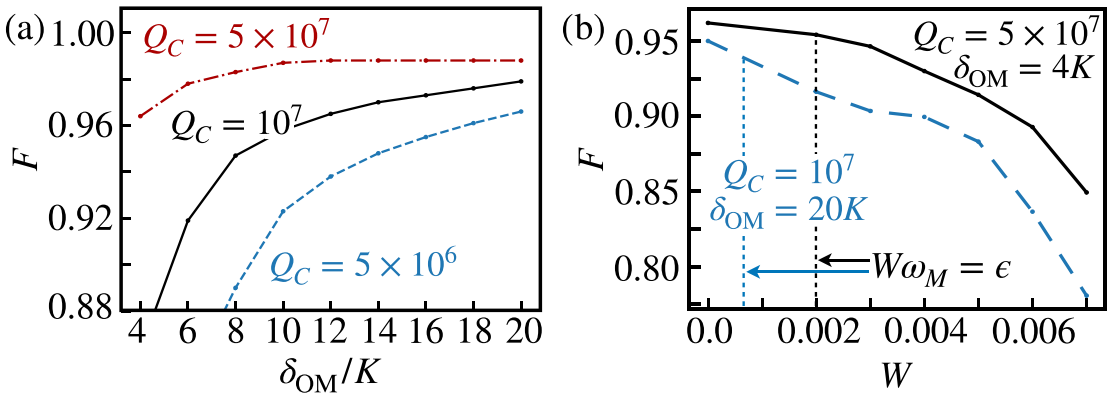

Figure 6. State transfer fidelity. (a) State transfer fidelity $F = |a_r(t_f)|^2$ as a function of δ_{OM} for optical quality factors $Q_C = 5.0 \times 10^6$, 10^7, 5×10^7. Here, $G = 2K$ and $Q_M = 10^6$. (b) Fidelity as a function of the disorder strength W for $G = 2K$, $\delta_{\mathrm{OM}} = 4K$ ($\delta_{\mathrm{OM}} = 20K$) and $Q_C = 5 \times 10^7$ ($Q_C = 10^7$) plotted in solid line (dashed). The vertical lines represent the disorder strengths for which $W\omega_M = \epsilon$ where $\epsilon/K = 1.0$ for $\delta_{\mathrm{OM}}/K = 4$ and $\epsilon/K = 0.34$ for $\delta_{\mathrm{OM}}/K = 20$. In all figures, we have considered $\omega_M/K = 460$, $\omega_C/K = 2 \times 10^6$, $J/K = 200$ and $g_{\mathrm{sp}}^{\mathrm{max}}/K = 0.06$.

randomly chosen from a uniform distribution ranging from $-W/2$ to $W/2$. The same form of local disorder are considered for $\Delta^{(j)}$, $G^{(j)}$, $\kappa_C^{(j)}$ and $\kappa_M^{(j)}$, where the upper script j refers to the jth OM cavity. In figure 6(b), we plot the state transfer fidelity as a function of W averaged over 50 realizations of disorders. We compare the robustness for $G = 2K$ and $\delta_{\mathrm{OM}} = 4K$, where the gap is $\epsilon = K$, to the scenario with $G = 2K$ and $\delta_{\mathrm{OM}} = 20K$, where the gap is $\epsilon \approx 0.34K$. The state-transfer fidelity starts to decrease for disorder strengths large enough to close the topological gap, which is roughly set by $W\omega_M \gtrsim \epsilon$ (as indicated by the vertical lines in figure 6(b)). An additional advantage of working with larger OM interactions is thus the increased resilience to disorder due to the larger gap.

Note that in order to consider the same disorder strength W for all the relevant parameters in the dynamics, we defined the disorder over the optical cavity frequencies in terms of the detuning $\Delta \sim J$ instead of the bare frequency $\omega_c \sim 10^4 J$. This means that the acceptable level of disorder $W \sim 0.01$ translates into relative variations of the cavity frequencies ω_c of about 10^{-3} percent. Reaching this level of precision is technically challenging, but since this is a common goal for many photonic crystal applications, a lot of efforts are currently focused on the development of photonic structures with significantly reduced levels of disorder. A promising direction are post-fabrication fine-tuning techniques, such as demonstrated in [69, 70], by which the required levels of accuracy can be reached.

5. Conclusion and outlook

In this work, we have proposed and analyzed a 2D hybrid system where the acoustic excitations within a Kagome lattice of coupled OM cavities interact with spin degrees of freedom of point defects. In this context, we have described the emergence of a topological phase where time-reversal symmetry is effectively broken for the acoustic excitations as a result of the interplay between the OM interaction and the inter-cavity hopping. As a potential application, we have shown that the resulting acoustic chiral edge states can serve as phononic quantum channels, which are purely unidirectional and robust with respect to onsite-disorder. Our analysis revealed how the key properties of such topological channels depend on the relevant OM coupling and detuning parameters and how an optimized trade-off between optical losses, propagation speed and disorder protection can be achieved. Apart from the considered example of SiV defects in diamond OM crystals, most of these considerations will be relevant as well for other types of qubits or other artificial realizations of topological systems.

Beyond quantum communication applications, the proposed hybrid system provides a versatile platform to study interacting quantum many-body systems, where topological phases with broken time-reversal symmetry are combined with strong nonlinearities provided by the spin qubits. The rich physics expected for such interacting topological insulators is still little understood and could be probed in such setting in various parameter regimes and employing only static spin-phonon interaction, which are in general much simpler to engineer.

Acknowledgments

M-AL thanks Dieter Jaksch for fruitful discussions. This research is supported by the National Research Foundation, Prime Minister's Office, Singapore and the Ministry of Education, Singapore under the Research Centres of Excellence programme. It was also partially funded by Polisimulator project co-financed by Greece and the EU Regional Development Fund, the European Research Council under the European Union's Seventh Framework Programme (FP7/2007-2013). PR acknowledges support from the Austrian Science Fund (FWF) through Grant No. P 32299-N27.

Appendix A. Rotating wave approximation and OM instability

For completeness, we remind here the Hamiltonian for the 2D OM array considered in the main text, which is given by ($\hbar = 1$)

$$\hat{H}_{\rm OMC} = \sum_j (\omega_M \hat{b}_j^\dagger \hat{b}_j - \Delta \hat{a}_j^\dagger \hat{a}_j + G e^{i\theta_j} \hat{a}_j^\dagger \hat{b}_j + G e^{-i\theta_j} \hat{b}_j^\dagger \hat{a}_j) + \sum_{\langle i,j\rangle} (K \hat{b}_i^\dagger \hat{b}_j + J \hat{a}_i^\dagger \hat{a}_j + \text{h.c.}). \tag{A.1}$$

All the parameters are defined in the main text.

To derive Hamiltonian (A.1), we have neglected the effects of the OM off-resonant parametric type terms

$$\sum_j G e^{-i\theta_j} \hat{a}_j \hat{b}_j + \text{h.c.} \tag{A.2}$$

Such terms describe the creation and annihilation of photon-phonon pairs and have been dropped during the derivation of equation (1) based on a rotating wave approximation. The processes that dominantly contribute to the corrections to the rotating wave approximation describe the creation (annihilation) of a phonon accompanied by the creation (annihilation) of a photon in the flat Kagome band. The typical oscillation frequency δ_K of these terms in the rotating frame is set by the distance of the flat optical band from its blue side band, $\delta_K \sim \delta_{\rm OM} + 2\omega_M$. As a consequence the leading order corrections to the RWA are of the order $\sim G/(\delta_{\rm OM} + 2\omega_M)$. It is important to keep in mind that contrary to the usual case of time-reversal preserving OM systems such terms can lead to an OM instability even in the regime where they represent a small perturbation and when the driving is red detuned compared to all optical resonances, see [54] for a detailed analysis. The reason for this behavior is that the same optical mode couples to different mechanical modes on its blue and red sidebands. As a consequence the mechanical modes that couple only to the blue sideband of the flat Kagome band but not to its red sideband are subject to a small overall optical induced amplification with rate $\sim \kappa_C G^2/\delta_K^2$. This implies that a small mechanical decay rate of the order $\kappa_M \sim \kappa_C G^2/(\delta_K)^2$ is required to stabilize the system, which is present for all parameter regimes considered in this manuscript.

Appendix B. Negatively charged silicon-vacancy centers in diamond

In this section we describe in more detail the negatively-charged silicon-vacancy center in diamond. More precisely, we focus on its electronic ground-state and its strain coupling to vibrational modes of its host crystal.

The molecular structure of the SiV center belongs to the D_{3d} point group symmetry and their electronic ground state are formed by an unpaired hole of spin $S = 1/2$ subjected to a strong spin–orbit interaction. The resulting fourfold ground state subspace is comprised of two doublets, $\{|1\rangle \simeq |e_-,\downarrow\rangle, |2\rangle \simeq |e_+,\uparrow\rangle\}$ and $\{|3\rangle \simeq |e_+,\downarrow\rangle, |4\rangle \simeq |e_-,\uparrow\rangle\}$, which are separated by $\Delta_{\rm SiV}/2\pi \simeq 46$ GHz [59, 60]. Here, $|e_\pm\rangle$ are eigenstates of the orbital quasi-angular momentum operator $\hat{L}_z$ associated to a $2\pi/3$ rotation about the symmetry axis of the defect (taken to be along z), i.e. $\hat{R}_{2\pi/3}|e_\pm\rangle = e^{-i\frac{2\pi}{3}\frac{\hat{L}_z}{\hbar}}|e_\pm\rangle = e^{\mp i\frac{2\pi}{3}}|e_\pm\rangle$. In the presence of a magnetic field $\vec{B} = B_0\vec{e}_z$, the Hamiltonian for a single SiV center is ($\hbar = 1$)

$$\begin{aligned}\hat{H}_{\rm SiV} = {} & \omega_B |2\rangle\langle 2| + \Delta_{\rm SiV}|3\rangle\langle 3| + (\Delta_{\rm SiV} + \omega_B)|4\rangle\langle 4| \\ & + \frac{1}{2}[\Omega(t) e^{i[\omega_d t + \phi(t)]}(|2\rangle\langle 3| + |1\rangle\langle 4|) + \text{h.c.}],\end{aligned} \tag{B.1}$$

where $\omega_B = \gamma_s B_0$ and γ_s is the spin gyromagnetic ratio. In equation (B.1), we have included a time-dependent driving field of frequency ω_d with a tunable Rabi-frequency $\Omega(t)$ and phase $\phi(t)$, which couples the lower and upper states of opposite spin. This drive can be implemented locally on individual defects either directly with a microwave field of frequency $\omega_d \sim \Delta_{\rm SiV}$ [71], or indirectly via an equivalent optical Raman process [28].

B.1. Strain coupling to mechanical modes

Within an OM cavity, we consider a single mechanical mode associated with a displacement profile $\vec{u}(\vec{r})$. In addition to modifying the indice of refraction seen by the optical mode, such deformation of the cavity modifies

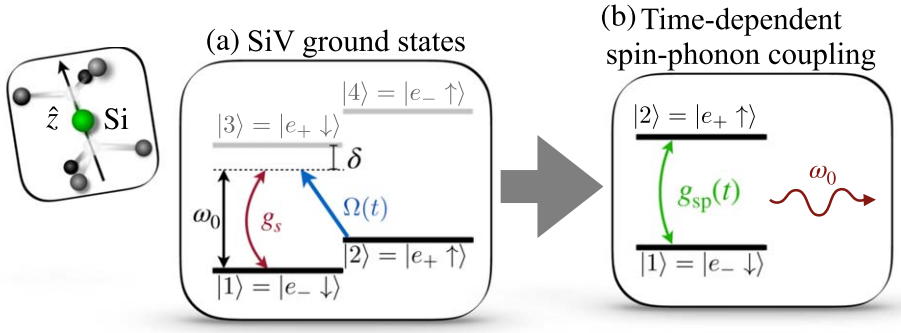

Figure B1. Silicon-vacancy center in diamond. (a) Energy structure of the SiV ground-state subspace where the two lowest-energy states $|1\rangle$ and $|2\rangle$ form a long-lived spin qubit. A microwave drive $\Omega(t)$ couples opposite spin states while the strain associated with a single phonon couples the orbital degrees of freedom $|e_\pm\rangle$ with strength g_s. The combination of the two processes leads to a tunable interaction between the spin states and phonons of frequency $\sim\omega_0$ as shown in (c).

the electronic environment seen by the SiV center, resulting in the coupling of its orbital states $|e_\pm\rangle$ [47, 48, 72]. The SiV-phonon coupling can be described by ($\hbar = 1$)

$$\hat{H}_{\rm int} = g_s \hat{J}_+ \hat{b} + \text{h.c.}, \tag{B.2}$$

where $\hat{J}_- = (\hat{J}_+)^\dagger = |1\rangle\langle 3| + |2\rangle\langle 4|$ is the spin-conserving lowering operator and g_s is the strain-induced coupling rate which is proportional to the local strain tensor $\epsilon^{ab}(\vec{r}) = \frac{1}{2}\left[\frac{\partial}{\partial x_b}u_a(\vec{r}) + \frac{\partial}{\partial x_a}u_b(\vec{r})\right]$. The resulting coupling rate can be written as $g_s = 2\pi d \frac{x_{\rm ZPF}}{\lambda_{\Delta_{\rm SiV}}}\xi(\vec{r}_{\rm SiV})$, where $d/2\pi \sim 1$ PHz is the strain sensitivity [47, 48], $x_{\rm ZPF} \sim 1$ fm is the mechanical zero point motion [63], $\lambda_{\Delta_{\rm SiV}} \sim 200$ nm the characteristic phonon wavelength in diamond and $\xi(\vec{r}_{\rm SiV})$ is the dimensionless strain distribution evaluated at the position of the SiV center $\vec{r}_{\rm SiV}$. From deformations $\vec{u}(\vec{r})$ observed in previous experiments [50] and state-of-the-art positioning of SiV defects [73], we expect $\xi(\vec{r}_{\rm SiV}) \sim 1$, leading to interaction rates as large as $g_s/2\pi \sim 30$ MHz. This estimation is consistent with finite-element simulations performed for 1D diamond nano-cavities [28]. For matching frequencies ($\Delta_{\rm SiV} = \omega_M$) and mechanical quality factors $Q \sim 10^5$, strong-coupling regime $g_s > \omega_M/Q$, $1/T_2^*$ should be reached, allowing coherent excitation transfer between the SiV center and the mechanical resonator.

B.2. Time-dependent effective spin-phonon coupling

In the specific case of a state transfer protocol, one has to control in time an effective coupling between the spin degree of freedom, encoded in the two lowest-energy ground-states $|1\rangle$ and $|2\rangle$, and the mechanical mode. This can be performed by an off-resonant driving of the state $|3\rangle$ (see figure B1 and equation (B.1)), leading to a standard three-level Λ atomic system. For large drive detunings $\delta = \omega_0 - \Delta_{\rm SiV}$, i.e. $|\delta| \gg |g_s|, |\omega_M - \omega_0|, |\Omega|$ with $\omega_0 = \omega_d + \omega_B$ the frequency of the emitted phonons, the higher-energy state $|3\rangle$ can be adiabatically eliminated resulting in an effective time-dependent spin-phonon coupling

$$g_{\rm sp}(t) = g_s \Omega(t)/\delta. \tag{B.3}$$

Assuming $0 \leqslant \Omega(t)/2\pi < 100$ MHz and $\delta/2\pi \lesssim 400$ MHz, this rate can be tuned between $g_{\rm sp} = 0$ and a maximal value of $g_{\rm sp}^{\rm max}/2\pi \sim 7$ MHz, which is still large enough to reach the strong coupling regime.

Appendix C. Diagonalization of the OM crystal Hamiltonian in the momentum space

In this appendix, we provide details of the diagonalisation in the quasi-momentum space of the OM Hamiltonian (1) in the case of an infinite 2D array and a semi infinite stripe. Focusing on the Kagome lattice architecture, the sum over all sites j of the crystal in equation (1) can be expanded into the sum over all unit cells of the triangular lattice and the three basis cavities within each cells, i.e. $j \to \{j, s\}$ corresponding to the cavity $s = \{A, B, C\}$ in the unit cell centered at $\vec{R}_j = m_j\vec{R}_1 + n_j\vec{R}_2$. Doing so, $\hat{H}_{\rm OMC}$ reads

$$\hat{H}_{\rm OMC} = \sum_{j,s}(\omega_M \hat{b}_{s,j}^\dagger \hat{b}_{s,j} - \Delta \hat{a}_{s,j}^\dagger \hat{a}_{s,j} + G e^{i\theta_s}\hat{a}_{s,j}^\dagger \hat{b}_{s,j} + G e^{-i\theta_s}\hat{b}_{s,j}^\dagger \hat{a}_{s,j}) + \sum_{n.n.}(K\hat{b}_{r,i}^\dagger \hat{b}_{s,j} + J\hat{a}_{r,i}^\dagger \hat{a}_{s,j} + \text{h.c.}). \tag{C.1}$$

Here, $\sum_{n.n.}$ represents the sum over the nearest neighbors.

C.1. Infinite 2D crystal

In the limit where the system is an infinite 2D array with $N \to \infty$ cavities, one can define

$$\hat{b}_s(\vec{k}) = \frac{1}{\sqrt{N}} \sum_j \mathrm{e}^{-\mathrm{i}\vec{k}\cdot\vec{R}_j} \hat{b}_{s,j}, \tag{C.2}$$

which destroys an excitation with the conserved quasi-momentum $\vec{k}$. The same definition applies for the optical modes, leading to

$$\hat{H}_{\mathrm{OMC}} = \sum_{\vec{k}} \hat{H}(\vec{k}) = \sum_{\vec{k}} \hat{H}_M(\vec{k}) + \hat{H}_C(\vec{k}) + \hat{H}_G(\vec{k}), \tag{C.3}$$

where the mechanical Hamiltonian

$$\begin{aligned}\hat{H}_M(\vec{k}) = \sum_s \omega_M \hat{b}_s^\dagger(\vec{k})\hat{b}_s(\vec{k}) + \{K(1+\mathrm{e}^{-\mathrm{i}\vec{k}\cdot\vec{R}_1})\hat{b}_A^\dagger(\vec{k})\hat{b}_B(\vec{k}) \\ + K(1+\mathrm{e}^{-\mathrm{i}\vec{k}\cdot[\vec{R}_1+\vec{R}_2]})\hat{b}_A^\dagger(\vec{k})\hat{b}_C(\vec{k}) + K(1+\mathrm{e}^{-\mathrm{i}\vec{k}\cdot\vec{R}_2})\hat{b}_B^\dagger(\vec{k})\hat{b}_C(\vec{k}) + \mathrm{h.c.}\}.\end{aligned} \tag{C.4}$$

Here, $\hat{b}_s^\dagger(\vec{k}) = [\hat{b}_s(\vec{k})]^\dagger$ and the equivalent form applies to the photons $\hat{H}_C(\vec{k})$. The OM interactions read

$$\hat{H}_G(\vec{k}) = G\sum_s \hat{b}_s^\dagger(\vec{k})\hat{a}_s(\vec{k})\mathrm{e}^{\mathrm{i}\theta_s} + \mathrm{h.c.} \tag{C.5}$$

Since H_{OMC} is quadratic, one can fully solve the excitation spectrum considering only a single excitation for which $\hat{H}(\vec{k})$ is a 6×6 matrix. Diagonalising $\hat{H}(\vec{k})$ for every $\vec{k}$ within the first Brillouin zone of the Kagome lattice leads to a six-band dispersion relation as shown in figure 2 of the main text.

C.2. Semi-infinite stripe

For a stripe that is infinite in the x direction (along $\vec{R}_2$) with N_y unit cells along $\vec{R}_1$, only the quasi momentum along x (k_x) is conserved and the proper expansion for $\hat{b}_{s,j}$ (same for $\hat{a}_{s,j}$) reads

$$\hat{b}_{s,j} = \frac{1}{\sqrt{N_x}} \sum_{k_x=-\pi/2a}^{\pi/2a} \mathrm{e}^{\mathrm{i}2nk_x a}\hat{b}_{s,m_j}(k_x). \tag{C.6}$$

Here $N_x \to \infty$ is the number of unit cells along x and $\hat{b}_{s,m}(k_x)$ is the destruction operator for a mechanical mode with quasi-momentum k_x in cavity s of the mth unit cell along $\vec{R}_1$. We thus consider a strip that goes from $y = 0$ to $y = -N_y\sqrt{3}\,a$ and increasing m means to go along $-y$.

Similar to the infinite 2D case, one gets

$$\hat{H}_{\mathrm{OMC}} = \sum_{k_x} \hat{H}(k_x) = \sum_{k_x} \hat{H}_M(k_x) + \hat{H}_C(k_x) + \hat{H}_G(k_x), \tag{C.7}$$

with

$$\begin{aligned}\hat{H}_M(k_x) = \sum_s \sum_{m=1}^{N_y} \omega_M \hat{b}_{s,m}^\dagger(k_x)\hat{b}_{s,m}(k_x) + K\sum_{m=1}^{N_y}\{\hat{b}_{A,m}^\dagger(k_x)[\hat{b}_{B,m-1}(k_x)\mathrm{e}^{2\mathrm{i}k_x a} + \hat{b}_{B,m}(k_x) \\ + \hat{b}_{C,m}(k_x) + \hat{b}_{C,m-1}(k_x)] + \hat{b}_{B,m}^\dagger(k_x)\hat{b}_{C,m}(k_x)[1 + \mathrm{e}^{-2\mathrm{i}k_x a}\} \\ + \hat{b}_{B,0}^\dagger(k_x)\hat{b}_{C,0}(k_x)[1+\mathrm{e}^{-2\mathrm{i}k_x a}] + \mathrm{h.c.}\end{aligned} \tag{C.8}$$

The last line describes the hoppings within the first unit cell and so determines the form of the edge. In that case, the site A is missing which leads to a straight edge as pictured in figure 4 of the main text. The optical Hamiltonian $\hat{H}_C(k_x)$ adopts the same form.

Within the single excitation subspace, H_{k_x} is a matrix of dimension $3N_y - 1$ and its diagonalisation leads to the dispersion relation shown in figure 3(a) of the main text. For finite G and a phase pattern $\Delta\theta = \pm 3\pi/2$, the edge states appear in the energy spectrum and can be expressed within the same basis, i.e.

$$\hat{b}_E(k_x) = \sum_{s,m} \mathrm{e}^{-\frac{ma}{\xi(k_x)}}\mathrm{e}^{-\mathrm{i}\phi_m(k_x)}[u_s\hat{b}_{s,m}(k_x) + v_s\hat{a}_{s,m}(k_x)]. \tag{C.9}$$

Here, the coefficients u_s and v_s are the mechanical and optical probability amplitudes on the basis s, respectively. The edge state decays exponentially within the bulk with a penetration depth $\xi(k_x)$ and phases $\phi_m(k_x)$.

Appendix D. Topological gap

In this section, we derive in more detail the effective models to describe the opening and closing of the topological gap. We consider an infinite 2D array and utilize the modes derived in equation (C.2).

As described in the main text, at the high symmetry points **K** and **K**′, the eigenstates of the Kagome lattice have also well-defined quasi-angular momentum (upon rotation of $2\pi/3$), i.e. $\hat{R}_{2\pi/3}|m_{\mathbf{K},\sigma}\rangle = \mathrm{e}^{-\mathrm{i}\sigma\frac{2\pi}{3\hbar}}|m_{\mathbf{K},\sigma}\rangle$ with $\sigma = \{-1, 0, 1\}$ (same for **K**′). In that case

$$\hat{b}_{\mathbf{K},\sigma} = \sum_j \frac{\mathrm{e}^{-\mathrm{i}\mathbf{K}\cdot\vec{R}_j}}{\sqrt{3N}}(\hat{b}_{A,j} + \mathrm{e}^{-\mathrm{i}\sigma 2\pi/3}\hat{b}_{B,j} + \mathrm{e}^{\mathrm{i}\sigma 2\pi/3}\hat{b}_{C,j}). \tag{D.1}$$

In addition, a phase pattern of the drive $\Delta\theta = \theta_A - \theta_B = \theta_B - \theta_C = \theta_C - \theta_A = \pm 2\pi/3$ means that only the optical mode $|o_{\mathbf{\Gamma},\pm}\rangle$ is driven.

Following the conservation of the total angular momentum, only few OM processes are allowed. For example, given $\Delta\theta = 2\pi/3$, the lowest-energy optical eigenstate is $|o_{\mathbf{K},+}\rangle$ and can only interact with the mechanical eigenstate $|o_{\mathbf{K},+}\rangle$ at the Dirac point $\omega_M + K$, leading to a simple two-mode effective model

$$H_{\mathrm{eff},\mathbf{K}} = \delta_{\mathrm{OM}} a^\dagger_{\mathbf{K},-} a_{\mathbf{K},-} + G(a^\dagger_{\mathbf{K},-} b_{\mathbf{K},+} + a_{\mathbf{K},-} b^\dagger_{\mathbf{K},+}). \tag{D.2}$$

Here $a_{\mathbf{K},-}$ destroys a photon in mode $|o_{\mathbf{\Gamma},\mp}\rangle$ and the effective Hamiltonian is written in a frame that rotates at the frequency $\omega_M + K$. Each time a phonon is destroyed, a photon of quasi-angular momentum $\sigma = +$ is also absorbed. $H_{\mathrm{eff},\mathbf{K}}$ is easily diagonalized and leads to

$$\epsilon = \frac{\delta_{\mathrm{OM}}}{2}\left(\sqrt{1 + \frac{4G^2}{\delta^2_{\mathrm{OM}}}} - 1\right). \tag{D.3}$$

Note that the highest mechanical band remains untouched with $E_{m,2}(\mathbf{K}) = \omega_M + K$.

For larger coupling rates G, processes occurring near quasi-momentum $\mathbf{M}_1$, $\mathbf{M}_2$ and $\mathbf{M}_3$ start to play a role (in what follows we omit the subscript for clarity). Those high-symmetry points are invariant under $\mathcal{C}_2$ rotations. As a consequence the normal modes are divided into symmetric and anti-symmetric normal modes at these points. For this reason the anti-symmetric mechanical band $E_{m,2}(\mathbf{M})$ do not interact with the symmetric optical band $E_{o,1}(\mathbf{M})$. The consequence is that no matter how large the gap at **K** and **K**′ becomes, the middle mechanical band stays at $E_{m,\mathbf{M}} = \omega_M$ and thus bounds the total gap at $\epsilon_{\max} = K$.

Moreover, the allowed interaction between the optical band $E_{o,1}(\mathbf{M})$ and the highest mechanical band $E_{m,3}(\mathbf{M})$ has the net effect to push down the mechanical band which closes the gap. In order to accurately capture the processes, we also need to include the lowest mechanical band, leading to a 3-mode effective model

$$H_{\mathrm{eff},\mathbf{M}} = \delta_{\mathrm{OM}} a^\dagger_{\mathbf{M},1} a_{\mathbf{M},1} - 3K b^\dagger_{\mathbf{M},1} b_{\mathbf{M},1} + \left(\frac{G}{2} a^\dagger_{\mathbf{M},1} b_{\mathbf{M},1} + \frac{\sqrt{3}G}{2} a^\dagger_{\mathbf{M},1} b_{\mathbf{M},3} + \mathrm{h.c.}\right). \tag{D.4}$$

From $H_{\mathrm{eff},\mathbf{M}}$, one can find the critical value G_c at which the gap starts to close, leading to the final expression

$$\epsilon = \mathrm{Min}\left[\frac{\delta_{\mathrm{OM}}}{2}\left(\sqrt{1 + \frac{4G^2}{\delta^2_{\mathrm{OM}}}} - 1\right), K\right], \tag{D.5}$$

for $G < G_c$, where

$$G_c/K = \sqrt{3\delta_{\mathrm{OM}}/2K}, \tag{D.6}$$

is the critical coupling above which the gap decreases.

Appendix E. State transfer in a 1D Markovian waveguide

In this section, we write a simple model for two TLS weakly coupled to a 1D chiral channel within the Born–Markov approximation. Doing so, we derive the effective transfer rate between the emitting TLS and the waveguide as well as the dissipation rates due to photons and phonons loss. For consistency, we remind here the form of the edge-state lowering operator

$$\hat{b}_E(k_x) = \sum_{s,m} \mathrm{e}^{-\frac{ma}{\xi(k_x)} - \mathrm{i}\phi_m(k_x)}[u_s(k_x)\hat{b}_{s,m}(k_x) + v_s(k_x)\hat{a}_{s,m}(k_x)]. \tag{E.1}$$

We connect the important results to the group velocity v_g, penetration depth ξ and optical fraction of the edge state P_{opt}, all shown in figure 4 of the main text. All the remaining parameters are defined in the main text.

We consider both the emitting and receiving defects, denoted by the subscripts $\{e, r\}$ respectively, to be localized in the outermost unit cells along the edge, i.e. $m = 0$ in equation (E.1). Only keeping the edge state from the OM array, we write the simplest Hamiltonian

$$\hat{H}_{\mathrm{1D}} = \hat{H}_{\mathrm{TLS}} + \hat{H}_E + \hat{H}_{\mathrm{int}} \tag{E.2}$$

with

$$\begin{aligned}\hat{H}_{\rm TLS} &= \frac{\omega_0}{2}(\sigma_{e,z} + \sigma_{r,z}),\\ \hat{H}_E &= \sum_{k_x} \omega_E(k_x) b_E^\dagger(k_x) b_E(k_x),\\ \hat{H}_{\rm int} &= \frac{1}{\sqrt{N_x}} \sum_{k_x} [u_{s_e}(k_x) \mathrm{e}^{2\mathrm{i}k_x j_e a} g_{\rm sp}^{(e)}(t) \sigma_{e,+} b_E(k_x)\\ &\quad + u_{s_r}(k_x) \mathrm{e}^{2\mathrm{i}k_x j_r a} g_{\rm sp}^{(r)}(t) \sigma_{r,+} b_E(k_x) + \text{h.c.}].\end{aligned} \tag{E.3}$$

Here j_e (j_r) and s_e (s_r) indicate the unit-cell position along the edge and which basis the emitting (receiving) TLS is coupled to, with corresponding coupling strength $g_{\rm sp}^{(e)}$ ($g_{\rm sp}^{(r)}$).

We consider the single-excitation ansatz

$$|\psi(t)\rangle = \alpha|0\rangle + \beta \mathrm{e}^{-\mathrm{i}\omega_0 t}\left[a_e(t)\sigma_{e,+} + a_r(t)\sigma_{r,+} + \sum_{k_x} a_{k_x}(t) b_E^\dagger(k_x)\right]|0\rangle, \tag{E.4}$$

where $|0\rangle$ represents the ground state of the whole system. The Schrödinger equation for the edge modes leads to

$$\begin{aligned}a_{k_x}(t) = \mathrm{e}^{-\mathrm{i}(\omega_E(k_x)-\omega_0)(t-t_0)} a_{k_x}(t_0) - \mathrm{i}\frac{1}{\sqrt{N_x}} \int_{t_0}^{t} \mathrm{d}\tau \mathrm{e}^{-\mathrm{i}(\omega_E(k_x)-\omega_0)(t-\tau)}\\ [u_{s_e}^*(k_x) \mathrm{e}^{-2\mathrm{i}k j_e a} g_{\rm sp}^{(e)*}(\tau) a_e(\tau) + u_{s_r}^*(k_x) \mathrm{e}^{-2\mathrm{i}k j_r a} g_{\rm sp}^{(r)*}(\tau) a_r(\tau)].\end{aligned} \tag{E.5}$$

Using this result in the equation for the receiver's cavity and performing a Born–Markov approximation, one recovers the standard equation

$$\partial_t a_r(t) = -\frac{\gamma_r(t)}{2} a_r(t) - \sqrt{\gamma_r(t)}\, \mathrm{e}^{\theta_r(t)} f_{\mathrm{in,r}}(t), \tag{E.6}$$

with the phase

$$\theta_\sigma(t) = \arg[g_{\rm sp}^{(\sigma)}(t)] + \phi_{m=0}. \tag{E.7}$$

The effective decay rate of the TLS into the waveguide reads

$$\gamma_\sigma(t) = \frac{2\pi}{N_x} |g_{\rm sp}^{(\sigma)}(t)|^2 \sum_{k_x} |u_{s_\sigma}(k_x)|^2 \delta(\omega_E(k_x) - \omega_0) = \frac{2|u_{s_\sigma}|^2}{v_g/a} |g_{\rm sp}^{(\sigma)}(t)|^2. \tag{E.8}$$

Here, $u_{s_\sigma} \equiv u_{s_\sigma}(k_x = k_0)$, $v_g \equiv v_g(k_x = k_0)$ and $\phi_{m=0} \equiv \phi_{m=0}(k_x = k_0)$, where the momentum k_0 is defined as $\omega_E(k_0) = \omega_0$, i.e. the momentum at which the frequency of the TLS crosses the dispersion relation of the edge modes. Note that the factor 2 in the second line of equation (E.8) comes from the distance of $2a$ between two unit cells in the Kagome lattice. For example, in cases where only the atoms B and C are excited along the straight edges, i.e. truly 1D limit, $u_{s_\sigma} = 1/\sqrt{2}$ and $\gamma = a|g_{\rm sp}|^2/v_g$, as expected in a 1D unidirectional waveguide. Finally, the incoming field reads

$$\begin{aligned}f_{\mathrm{in,r}}(t) &= f_{\mathrm{out,e}}(t-\tau_{er}) \mathrm{e}^{\mathrm{i}\phi_{er}}\\ &= [f_{\mathrm{in,e}}(t-\tau_{er}) + \sqrt{\gamma_e(t-\tau_{er})}\, \mathrm{e}^{-\mathrm{i}\theta_e(t-\tau_{er})} a_e(t-\tau_{er})] \mathrm{e}^{\mathrm{i}\phi_{er}},\end{aligned} \tag{E.9}$$

with the propagation time and phase

$$\tau_{er} = 2(j_r - j_e)a/v_g, \qquad \phi_{er} = 2k_0(j_r - j_e)a. \tag{E.10}$$

This result is expected from the input–output formalism.

The role of the penetration depth $\xi \equiv \xi(k_x = k_0)$ is implicitly included in the coefficients u_{s_σ} as the normalization constraint imposes

$$\sum_{s,m} |u_{s_\sigma}^2| \mathrm{e}^{-\frac{2ma}{\xi}} \equiv 1. \tag{E.11}$$

As expected, as the penetration depth increases, the strength at which the TLS couples to the edge state decreases.

ORCID iDs

Marc-Antoine Lemonde https://orcid.org/0000-0002-6215-4932

References

[1] Wendin G 2017 Quantum information processing with superconducting circuits: a review *Rep. Prog. Phys.* **80** 106001
[2] Bloch I, Dalibard J and Zwerger W 2008 Many-body physics with ultracold gases *Rev. Mod. Phys.* **80** 885
[3] Gross C and Bloch I 2017 Quantum simulations with ultracold atoms in optical lattices *Science* **357** 995
[4] Bruzewicz C D, Chiaverini J, McConnell R and Sage J M Trapped-ion quantum computing: progress and challenges arXiv:1904.04178
[5] Saffman M, Walker T G and Mølmer K 2010 Quantum information with Rydberg atoms *Rev. Mod. Phys.* **82** 2313
[6] Neumann P *et al* 2010 Quantum register based on coupled electron spins in a room-temperature solid *Nat. Phys.* **6** 249
[7] Weber J R, Koehl W F, Varley J B, Janotti A, Buckley B B, Van de Walle C G and Awschalom D D 2010 Quantum computing with defects *PNAS* **107** 8513
[8] Yao N Y, Jiang L, Gorshkov A V, Maurer P C, Giedke G, Cirac J I and Lukin M D 2012 Scalable architecture for a room temperature solid-state quantum information processor *Nat. Commun.* **3** 800
[9] Cai J, Retzker A, Jelezko F and Plenio M B 2013 A large-scale quantum simulator on a diamond surface at room temperature *Nat. Phys.* **9** 168
[10] Wang Y *et al* 2015 Quantum simulation of helium hydride cation in a solid-state spin register *ACS Nano* **9** 7769
[11] Wallquist M, Hammerer K, Rabl P, Lukin M and Zoller P 2009 Hybrid quantum devices and quantum engineering *Phys. Scr.* **T137** 014001
[12] Xiang Z-L, Ashhab S, You J Q and Nori F 2013 Hybrid quantum circuits: superconducting circuits interacting with other quantum systems *Rev. Mod. Phys.* **85** 623
[13] Kurizki G, Bertet P, Kubo Y, Mølmer K, Petrosyan D, Rabl P and Schmiedmayer J 2015 Quantum technologies with hybrid systems *PNAS* **112** 3866
[14] Rabl P, Kolkowitz S J, Koppens F H, Harris J G E, Zoller P and Lukin M D 2010 A quantum spin transducer based on nanoelectromechanical resonator arrays *Nat. Phys.* **6** 602
[15] Stannigel K, Rabl P, Sørensen A S, Zoller P and Lukin M D 2010 Optomechanical transducers for long-distance quantum communication *Phys. Rev. Lett.* **105** 220501
[16] Schuetz M J A, Kessler E M, Giedke G, Vandersypen L M K, Lukin M D and Cirac J I 2015 Universal quantum transducers based on surface acoustic waves *Phys. Rev.* X **5** 031031
[17] Bochmann J, Vainsencher A, Awschalom D D and Cleland A N 2013 Nanomechanical coupling between microwave and optical photons *Nat. Phys.* **9** 712
[18] Bagci T *et al* 2014 Optical detection of radio waves through a nanomechanical transducer *Nature* **507** 81
[19] Andrews R W, Peterson R W, Purdy T P, Cicak K, Simmonds R W, Regal C A and Lehnert K W 2014 Bidirectional and efficient conversion between microwave and optical light *Nat. Phys.* **10** 321
[20] Rueda A *et al* 2016 Efficient microwave to optical photon conversion: an electro-optical realization *Optica* **3** 597
[21] Tian L 2015 Optoelectromechanical transducer: reversible conversion between microwave and optical photons *Ann. Phys.* **527** 1
[22] Treutlein P, Genes C, Hammerer K, Poggio M and Rabl P 2014 Hybrid mechanical systems *Cavity Optomechanics. Quantum Science and Technology* ed M Aspelmeyer *et al* (Berlin: Springer)
[23] Safavi-Naeini A H and Painter O 2011 Proposal for an optomechanical traveling wave phonon-photon translator *New J. Phys.* **13** 013017
[24] Khanaliloo B, Jayakumar H, Hryciw A C, Lake D P, Kaviani H and Barclay P E 2015 Single-crystal diamond nanobeam waveguide optomechanics *Phys. Rev.* X **5** 041051
[25] Patel R N, Wang Z, Jiang W, Sarabalis C J, Hill J T and Safavi-Naeini A H 2018 Single-mode phononic wire *Phys. Rev. Lett.* **121** 040501
[26] Habraken S J M, Stannigel K, Lukin M D, Zoller P and Rabl P 2012 Continuous mode cooling and phonon routers for phononic quantum networks *New J. Phys.* **14** 115004
[27] Gustafsson M V, Aref T, Frisk Kockum A, Ekström M K, Johansson G and Delsing P 2014 Propagating phonons coupled to an artificial atom *Science* **346** 207
[28] Lemonde M-A, Meesala S, Sipahigil A, Schuetz M J A, Lukin M D, Loncar M and Rabl P 2018 Phonon networks with silicon-vacancy centers in diamond waveguides *Phys. Rev. Lett.* **120** 213603
[29] Bienfait A *et al* 2019 Phonon-mediated quantum state transfer and remote qubit entanglement *Science* **364** 368
[30] Bennett S D, Yao N Y, Otterbach J, Zoller P, Rabl P and Lukin M D 2013 Phonon-induced spin-spin interactions in diamond nanostructures: application to spin squeezing *Phys. Rev. Lett.* **110** 156402
[31] Albrecht A, Retzker A, Jelezko F and Plenio M B 2013 Coupling of nitrogen vacancy centres in nanodiamonds by means of phonons *New J. Phys.* **15** 083014
[32] Lee D, Lee K W, Cady J V, Ovartchaiyapong P and Jayich A C B 2017 Topical review: spins and mechanics in diamond *J. Opt.* **19** 033001
[33] Kuzyk M C and Wang H 2018 Scaling phononic quantum networks of solid-state spins with closed mechanical subsystems *Phys. Rev.* X **8** 041027
[34] Li P-B, Li X-X and Nori F Band-gap-engineered spin-phonon, and spin-spin interactions with defect centers in diamond coupled to phononic crystals arXiv:1901.04650
[35] Cirac J I, Zoller P, Kimble H J and Mabuchi H 1997 Quantum state transfer and entanglement distribution among distant nodes in a quantum network *Phys. Rev. Lett.* **78** 3221
[36] Chang D E, Safavi-Naeini A H, Hafezi M and Painter O 2011 Slowing and stopping light using an optomechanical crystal array *New J. Phys.* **13** 023003
[37] Heinrich G, Ludwig M, Qian J, Kubala B and Marquardt F 2011 Collective dynamics in optomechanical arrays *Phys. Rev. Lett.* **107** 43603
[38] Xuereb A, Genes C and Dantan A 2012 Collective dynamics in optomechanical arrays *Phys. Rev. Lett.* **109** 223601
[39] Chen W and Clerk A 2014 Photon propagation in a one-dimensional optomechanical lattice *Phys. Rev.* A **89** 2033854
[40] Schmidt M, Kessler S, Peano V, Painter O and Marquardt F 2015 Optomechanical creation of magnetic fields for photons on a lattice *Optica* **7** 635
[41] Mathew J P, del Pino J and Verhagen E Synthetic gauge fields for phonon transport in a nano-optomechanical system arXiv:1812.09369
[42] MacQuarrie E R, Gosavi T A, Jungwirth N R, Bhave S A and Fuchs G D 2013 Mechanical spin control of nitrogen-vacancy centers in diamond *Phys. Rev. Lett.* **111** 227602
[43] Ovartchaiyapong P, Lee K W, Myers B A and Bleszynski Jayich A C 2014 Dynamic strain-mediated coupling of a single diamond spin to a mechanical resonator *Nat. Commun.* **5** 4429

[44] Barfuss A, Teissier J, Neu E, Nunnenkamp A and Maletinsky P 2015 Strong mechanical driving of a single electron spin *Nat. Phys.* **11** 820
[45] Golter D A, Oo T, Amezcua M, Stewart K A and Wang H 2016 Optomechanical quantum control of a nitrogen-vacancy center in diamond *Phys. Rev. Lett.* **116** 143602
[46] Meesala S, Sohn Y-I, Atikian H A, Kim S, Burek M J, Choy J T and Loncar M 2016 Enhanced strain coupling of nitrogen-vacancy spins to nanoscale diamond cantilevers *Phys. Rev. Appl.* **5** 034010
[47] Jahnke K D, Sipahigil A, Binder J M, Doherty M W, Metsch M, Rogers L J, Manson N B, Lukin M D and Jelezko F 2015 Electron–phonon processes of the silicon-vacancy centre in diamond *New J. Phys.* **17** 043011
[48] Sohn Y-I *et al* 2018 Controlling the coherence of a diamond spin qubit through its strain environment *Nat. Commun.* **9** 2012
[49] Meesala S *et al* 2018 Strain engineering of the silicon-vacancy center in diamond *Phys. Rev.* B **97** 205444
[50] Safavi-Naeini A H, Alegre T P M, Winger M and Painter O 2010 Optomechanics in an ultrahigh-Q two-dimensional photonic crystal cavity *Appl. Phys. Lett.* **97** 181106
[51] Gavartin E, Braive R, Sagnes I, Arcizet O, Beveratos A, Kippenberg T and Robert-Philip I 2011 Optomechanical coupling in a two-dimensional photonic crystal defect cavity *Phys. Rev. Lett.* **106** 203902
[52] Safavi-Naeini A H, Hill J T, Meenehan S, Chan J, Gröblacher S and Painter O 2014 Two-dimensional phononic-photonic band gap optomechanical crystal cavity *Phys. Rev. Lett.* **112** 153603
[53] Kalaee M, Paraïso T K, Pfeifer H and Painter O 2016 Design of a quasi-2D photonic crystal optomechanical cavity with tunable, large x^2-coupling *Opt. Express* **24** 21308
[54] Peano V, Brendel C, Schmidt M and Marquardt F 2015 Topological phases of sound and light *Phys. Rev.* X **5** 031011
[55] Ozawa T *et al* 2019 Topological photonics *Rev. Mod. Phys.* **91** 015006
[56] Barik S, Karasahin A, Flower C, Cai T, Miyake H, DeGottardi W, Hafezi M and Waks E 2018 A topological quantum optics interface *Science* **359** 6376
[57] Yao N Y, Laumann C R, Gorshkov A V, Weimer H, Jiang L, Cirac J I, Zoller P and Lukin M D 2013 Topologically protected quantum state transfer in a chiral spin liquid *Nat. Commun.* **4** 1585
[58] Goss J P, Jones R, Breuer S J, Briddon P R and Öberg S 1996 The Twelve-Line 1.682 eV luminescence center in diamond and the vacancy-silicon complex *Phys. Rev. Lett.* **77** 3041
[59] Hepp C *et al* 2014 Electronic structure of the silicon vacancy color center in diamond *Phys. Rev. Lett.* **112** 036405
[60] Hepp C 2014 Electronic structure of the silicon vacancy color center in diamond *PhD Thesis* University of Saarland
[61] Sukachev D D, Sipahigil A, Nguyen C T, Bhaskar M K, Evans R E, Jelezko F and Lukin M D 2017 The silicon-vacancy spin qubit in diamond: quantum memory exceeding ten milliseconds and single-shot state readout *Phys. Rev. Lett.* **119** 223602
[62] Becker J N and Becher C 2017 Coherence properties and quantum control of silicon vacancy color centers in diamond *Phys. Status Solidi* a **214** 1700586
[63] Safavi-Naeini A H and Painter O 2010 Design of optomechanical cavities and waveguides on a simultaneous bandgap phononic-photonic crystal slab *Opt. Express* **18** 926
[64] Aspelmeyer M, Kippenberg T J and Marquardt F 2014 Cavity optomechanics *Rev. Mod. Phys.* **86** 1391
[65] Haldane F D M 1988 Model for a quantum hall effect without landau levels: condensed-matter realization of the 'Parity Anomaly' *Phys. Rev. Lett.* **61** 2015
[66] Thouless D J, Kohmoto M, Nightingale M P and den Nijs M 1982 Quantized Hall conductance in a two-dimensional periodic potential *Phys. Rev. Lett.* **49** 405
[67] Brendel C, Peano V, Painter O J and Marquardt F 2017 Pseudomagnetic fields for sound at the nanoscale *PNAS* **114** 3390
[68] Burek M J *et al* 2016 Diamond optomechanical crystals *Optica* **3** 1404
[69] Sokolov S, Lian J, Yuce E, Combrie S, De Rossi A and Mosk A P 2017 Tuning out disorder-induced localization in nanophotonic cavity arrays *Opt. Express* **25** 4598
[70] Sumetsky M and Dulashko Y 2012 SNAP: fabrication of long coupled microresonator chains with sub-angstrom precision *Opt. Express* **20** 27896
[71] Pla J J, Tan K Y, Dehollain J P, Lim W H, Morton J J L, Jamieson D N, Dzurak A S and Morello A 2012 A single-atom electron spin qubit in silicon *Nature* **489** 541
[72] Kepesidis K V, Lemonde M-A, Norambuena A, Maze J R and Rabl P 2016 Cooling phonons with phonons: acoustic reservoir engineering with silicon-vacancy centers in diamond *Phys. Rev.* B **94** 214115
[73] Schröder T *et al* 2017 Scalable focused ion beam creation of nearly lifetime-limited single quantum emitters in diamond nanostructures *Nat. Commun.* **8** 15376